Martinez Garzon, P., Kwiatek, G., Sone, H., Bohnhoff, M., Dresen, G., Hartline, C. (2014): Spatiotemporal changes, faulting regimes, and source parameters of induced seismicity: A case study from The Geysers geothermal field. - *Journal of Geophysical Research*, *119*, 11, p. 8378-8396.

DOI: http://doi.org/10.1002/2014JB011385

AGU PUBLICATIONS

JGR

Journal of Geophysical Research: Solid Earth

RESEARCH ARTICLE
10.1002/2014JB011385

Key Points:
- Geothermal reservoir characterization from microseismicity and geomechanics
- Systematic relation between injection rates and seismic parameters
- Thermal and pore pressure effects are the mechanisms driving the seismicity

Correspondence to:
P. Martínez-Garzón,
patricia@gfz-potsdam.de

Citation:
Martínez-Garzón, P., G. Kwiatek, H. Sone, M. Bohnhoff, G. Dresen, and C. Hartline (2014), Spatiotemporal changes, faulting regimes, and source parameters of induced seismicity: A case study from The Geysers geothermal field, *J. Geophys. Res. Solid Earth*, *119*, 8378–8396, doi:10.1002/2014JB011385.

Received 13 JUN 2014
Accepted 13 OCT 2014
Accepted article online 17 OCT 2014
Published online 25 NOV 2014

Spatiotemporal changes, faulting regimes, and source parameters of induced seismicity: A case study from The Geysers geothermal field

Patricia Martínez-Garzón[1], Grzegorz Kwiatek[1], Hiroki Sone[1], Marco Bohnhoff[1,2], Georg Dresen[1,3], and Craig Hartline[4]

[1]Helmholtz-Centre Potsdam GFZ German Research Centre for Geosciences, Potsdam, Germany, [2]Institute of Geological Sciences, Free University Berlin, Berlin, Germany, [3]Institute of Earth and Environmental Sciences, University of Potsdam, Potsdam, Germany, [4]Calpine Corporation, Middletown, California, USA

Abstract The spatiotemporal, kinematic, and source characteristics of induced seismicity occurring at different fluid injection rates are investigated to determine the predominant physical mechanisms responsible for induced seismicity at the northwestern part of The Geysers geothermal field, California. We analyze a relocated hypocenter catalog from a seismicity cluster where significant variations of the stress tensor orientation were previously observed to correlate with injection rates. We find that these stress tensor orientation changes may be related to increased pore pressure and the corresponding changes in poroelastic stresses at reservoir depth. Seismic events during peak injections tend to occur at greater distances from the injection well, preferentially trending parallel to the maximum horizontal stress direction. In contrast, at lower injection rates the seismicity tends to align in a different direction which suggests the presence of a local fault. During peak injection intervals, the relative contribution of strike-slip faulting mechanisms increases. Furthermore, increases in fluid injection rates also coincide with a decrease in *b* values. Our observations suggest that regardless of the injection stage, most of the induced seismicity results from thermal fracturing of the reservoir rock. However, during peak injection intervals, the increase in pore pressure may likewise be responsible for the induced seismicity. By estimating the thermal and hydraulic diffusivities of the reservoir, we confirm that the characteristic diffusion length for pore pressure is much greater than the corresponding length scale for temperature and also more consistent with the spatial extent of seismicity observed during different injection rates.

1. Introduction

The mitigation of Induced Seismicity (IS) caused by fluid injection into geo-reservoirs has recently become a topic of increasing concern when considering efficient and sustainable energy production [e.g., *Ellsworth*, 2013]. Reservoir stimulation is a common practice in geothermal energy projects as well as in production of conventional and unconventional hydrocarbons (e.g., shale gas). However, it involves the injection of large amounts of fluids frequently resulting in increased seismic activity and nonnegligible seismic hazard in the surrounding areas [*Dost and Haak*, 2007; *McGarr*, 2014]. An improved understanding of the physical processes governing IS and their relation to geomechanical reservoir conditions (e.g., stress, pore fluid pressure) and hydraulic parameters (e.g., injection rates) is of practical importance for reservoir operators and local communities [*Majer et al*., 2007; *Evans et al*., 2012].

The mechanisms for occurrence of IS seismicity in geo-reservoirs undergoing fluid injection have been investigated from both field observations and theoretical studies. Pore pressure increase due to fluid injection reducing effective stresses may reactivate shearing on small preexisting faults and fractures favorably oriented with respect of the stress field and trigger microseismic events [e.g., *Majer et al*., 2007]. The fluid propagates away from the injection well through the rock matrix or along conductive fractures. Frequently, fluid-injection induced seismicity clusters form an ellipsoidal shape that is preferentially elongated along the orientation of the maximum horizontal stress (e.g., Soultz-sous-Forêts, France) [*Cuenot et al*., 2006]. *Shapiro et al*. [1999, 2003] explained this to reflect an anisotropic hydraulic diffusivity. *Schoenball et al*. [2010] showed from numerical studies that anisotropy of the stress field may also result in an ellipsoidal shape of the seismicity cloud. Pore pressure and stress tensor are coupled in such a way that poroelastic stress changes may even modify the local tectonic faulting regime [*Altmann et al*., 2014]. Additionally, natural geothermal reservoirs or Enhanced Geothermal Systems (EGS) are developed in high-temperature environments. Here thermoelastic stresses

induced by the injection of cool water in the high-temperature reservoir rock are considered a prominent cause inducing seismicity, especially near the injection wells and the steam-producing fractures [e.g., *Segall and Fitzgerald*, 1998; *Rutqvist et al*., 2013]. Due to cooling, the reservoir rock experiences contractional strain perturbing the stress field and thus inducing microseismicity. This mechanism has been proposed to be dominant at The Geysers geothermal field (California, USA), where recent thermal, mechanical, and hydraulic modeling of an EGS have suggested that the microseismicity was governed mainly by thermoelastic effects from the reservoir cooling around the injection well plus small poroelastic stress changes [*Rutqvist et al*., 2013]. While poroelastic and thermoelastic effects likely occur concurrently, the temporal and spatial extent at which these mechanisms govern the induced seismicity in geothermal reservoirs needs to be further investigated from field data.

Advanced IS waveform processing techniques allow identifying the active reservoir fracture network and monitoring geomechanical processes occurring in a reservoir due to fluid injection. In particular, the double-difference relocation of IS hypocenters may help revealing in small-scale patterns of the spatiotemporal distribution of seismicity [*Waldhauser and Ellsworth*, 2000]. The method allows tracing potential migration of seismic events in the vicinity of the well during injection and after shut-in [e.g., *Kwiatek et al*., 2013, 2014; *Albaric et al*., 2014]. The spatiotemporal evolution of IS has been described using observed triggering and back-fronts of the seismicity [*Shapiro et al*., 2002; *Parotidis et al*., 2004]. Furthermore, calculation of seismic source mechanisms combined with stress inversion provides information on the orientation and relative magnitudes of principal stresses in a reservoir and the potential seismic hazard associated with stimulation [e.g., *Schoenball et al*., 2014]. Analyses of faulting kinematics have been performed for an EGS, e.g., at Soultz-sous-Forêts, France by *Cuenot et al*. [2006]. They found that most of the IS events likely represent normal faulting mechanisms, while the occurrence of strike-slip events was limited to the deepest part of the stimulated volume, illustrating the spatially heterogeneous nature of faulting style within a stimulated volume. Additional information on seismic faulting processes is provided by analysis of earthquake source parameters and statistical attributes of earthquake populations, for example, Gutenberg-Richter magnitude-frequency distribution. *Bachmann et al*. [2012] reported a decrease of *b* values with distance from the injection well at the Deep Heat Mining project in Basel/Switzerland. Also, an increase of the static stress drop with distance from the injection well has been reported for the same site [*Goertz-Allmann et al*., 2011] as well as for the Berlín Geothermal field, El Salvador [*Kwiatek et al*., 2014].

The motivation for the analysis presented here originated from a previous study of *Martínez-Garzón et al*. [2013] who observed significant rotations in the orientation of principal stresses in response to changes in the fluid injection rates at The Geysers geothermal field, California. From inversion of focal mechanisms it was observed that the vertical principal stress (the σ_1 axis) tilted toward the NE/SW by approximately 20° when injection rates were at their peak level (peak injection). The stress rotations were initially interpreted to be caused either by reactivation of preexisting fractures with a more transtensional component or due to potential tensile opening of new fractures. Although further analysis was necessary to determine the exact physical mechanism, the study demonstrated the close relation between reservoir stress state and fluid injection rate.

In this study, we analyze potential local short-term effects of peak-fluid injections on the source characteristics of microseismicity induced during two injection periods at the same site as presented in *Martínez-Garzón et al*. [2013] in order to gain insights on the physical mechanisms leading to the occurrence of seismicity. First, we create an improved seismicity catalog by relocating the seismicity and calculate the corresponding fault plane solutions. Then, we investigate potential variations in the faulting kinematics, spatiotemporal distribution of hypocenters, temporal changes in *b* values, maximum earthquake magnitude, static stress drop, and relative stress magnitudes from the induced seismicity. The obtained results suggest that different physical mechanisms of IS can operate at different temporal and spatial scales depending on the fluid injection rate. To support our findings, we estimate the reservoir permeability, hydraulic and thermal diffusivities, and stress magnitudes. The results presented here aim at improving reservoir characterization and understanding the physics governing stimulation-induced seismicity.

2. The Geysers Geothermal Field

The Geysers (TG) geothermal field in Northern California, USA, is the largest producing geothermal field in the world with approximately 330 active steam production wells and 60 active water injection wells [*Brophy et al*., 2010]. This vapor-dominated reservoir has been producing since the 1960s, achieving

maximum production in 1987. Since then, the reservoir production has been slowly declining [*Gunasekera et al*., 2003; *Majer and Peterson*, 2007]. The decay was caused primarily by the decrease in reservoir pressure, along with some cooling of the reservoir [*Mossop and Segall*, 1997]. To stabilize the reservoir pressure and preserve the steam production, large volumes of fluid have been injected with the construction of pipelines supplying treated waste water from Lake County since 1997 and Sonoma County since 2003 [*Majer and Peterson*, 2007; *Majer et al*., 2007]. Associated with the reservoir pressure decline, GPS surveys indicate surface subsidence above the reservoir at a rate of approximately 5 cm/yr during the years 1977–1996 [*Mossop and Segall*, 1997].

The Geysers geothermal field exists within a complex assemblage of Franciscan rocks (200 to 80 Ma in age) representing the ancient Farallon plate subduction complex. These Franciscan rocks consist primarily of greywacke forming part of a complex assemblage of intensely deformed, faulted, and sheared metamorphic rocks. A transition from subduction to right-lateral strike-slip faulting began about 30 Ma ago as the spreading center between the Pacific Plate (to the west) and the Farallon Plate (to the east) was subducted beneath the North American continent. Since this transition, right-lateral strike-slip motion along the broader San Andreas Fault Zone system accommodates the relative motion between the Pacific Plate and North American Plate [*DeCourten*, 2008]. The right-lateral strike-slip motion of nearly parallel faults at progressively slower rates to the east resulted in the transtensional tectonic environment between the (now inactive) Macaama and Collayomi faults associated with the development of The Geysers geothermal system. Here approximately 1.1 Ma ago, a 760°C granitic intrusion (the "Felsite") resulted in contact metamorphism and fracturing of the Franciscan complex at depth. Magmatic and hydrothermal gases, reacting with deeply circulating ground water with dissolved silica, formed the reservoir caprock. More recently (~0.25 Ma) the initial approximately 300°C liquid-dominated geothermal reservoir developed into the modern (preproduction) 240°C/3.5 MPa vapor-dominated Geysers geothermal reservoir with renewed heating by additional magmatic intrusions, some possibly as recent as 0.01 Ma [*Hulen et al*., 1997a, 1997b; *Moore et al*., 2000].

The low-permeability, highly fractured reservoir rocks (greywacke) have a low total porosity of about 1–2% [*Barker et al*., 1992], reservoir temperatures of approximately 240°C at 2 km depth [*García et al*., 2012], and temperatures exceeding 350°C in the northwest Geysers at depths below ~2.75 km (high-temperature zone, *Jeanne et al*. [2014]). At TG, water is injected into the reservoir to prevent reservoir depletion. In this process, relatively cool surface water falls freely into the "injection" well resulting in significant volume reduction as the reservoir steam condenses. This causes negative gauge pressure at the wellhead, in contrast to active surface pumping commonly performed for reservoir stimulation with injection at elevated wellhead pressures.

The induced seismicity occurring throughout the geothermal field has been attributed to both water injection and steam production [*Eberhart-Phillips and Oppenheimer*, 1984; *Oppenheimer*, 1986; *Foulger et al*., 1997]. Since a dense local seismic network was deployed in 2003, approximately 4000 seismic events per year with magnitudes between 1.0 and 4.5 have been observed. Within The Geysers, estimations from focal mechanisms of seismicity on the local maximum horizontal stress (S_{HMax}) are generally consistent with the NNE-SSW trending orientation of the regional geological structures [*Oppenheimer*, 1986; *Provost and Houston*, 2003], suggesting that the tectonic stresses in the region are much larger than the local stress perturbations induced by geothermal activities. Recent results from *Altmann et al*. [2013] suggest that tectonic loading contributes little within the reservoir compared to the pore pressure diffusion on timescales of several years.

Different physical processes have been proposed to explain the occurrence of IS [*Allis*, 1982; *Majer et al*., 2007]. Thermal fracturing of the hot reservoir rocks due to the local and rapid contraction during relatively cool water injection is considered to be a prominent mechanism producing microseismicity [*Segall and Fitzgerald*, 1998; *Rutqvist et al*., 2013]. Additionally, changes in the pore pressure from both fluid injection and/or reservoir depletion may lead to perturbation of effective stresses in the reservoir resulting in seismic activity. Lastly, induced seismicity due to geochemical alteration of the rocks during cooling has also been proposed [*Allis*, 1982].

Progressive reservoir depletion has been proposed based on declining steam production in conjunction with subsidence at the surface [*Gunasekera et al*., 2003; *Vasco et al*., 2013]. However, most of the NW part of the field was practically not exploited until 2007. To recharge the reservoir and reduce noncondensable gas concentrations, some water injection projects were established resulting in induced seismicity. Analysis of fault plane solutions of seismicity occurring in the NW Geysers shows a consistent N/NE orientation for the maximum horizontal stress, indicating a combined normal and strike-slip faulting regime [*Boyle and Zoback*, 2014].

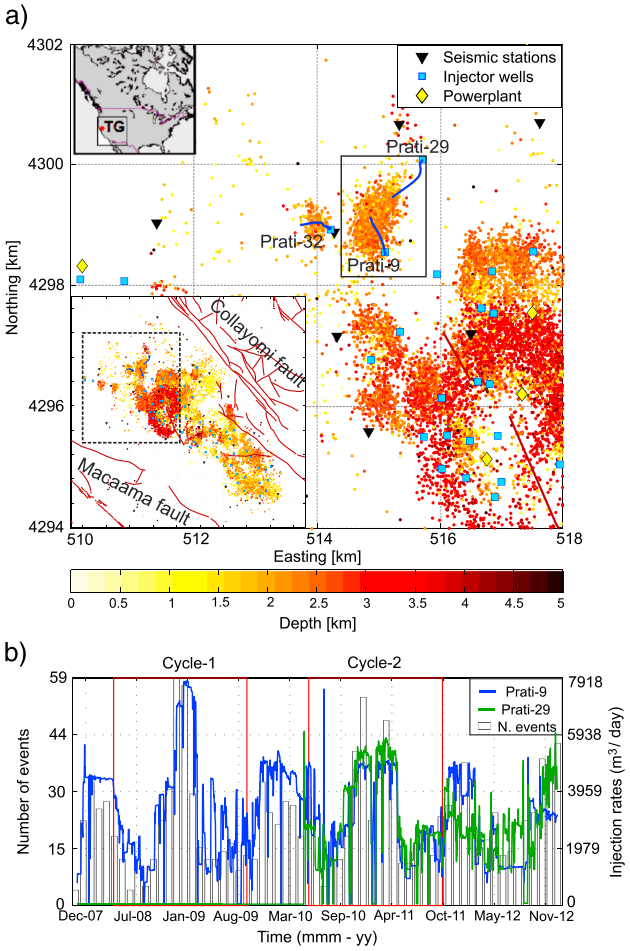

Figure 1. (a) Map views of seismicity for The Geysers geothermal field between 2007 and 2012 (locations from NCEDC). Location of TG in North America (top left). TG map view of the entire reservoir (bottom left). The dashed square is enlarged within the main map. Depth of the seismicity is color scaled. The trajectory of particular wells is plotted in blue. The analyzed cluster in this study appears within the black rectangle in the main figure. Brown lines are faults mapped by U.S. Geological Survey. (b) Monthly number of events and daily injection data for the wells Prati-9 and Prati-29 between November 2007 and December 2012. Red rectangles frame the two injection cycles that will be here interpreted in detail.

Additionally, source parameters estimation of microearthquakes ($M < 3$) in this part of the field revealed average stress drops of 11 MPa, which is comparable to the stress drops of natural tectonic earthquakes occurring in the area [*Viegas and Hutchings*, 2011].

3. Data and Methodology Used

We analyzed the seismic data from the most prominent and spatially isolated cluster of IS in the northwestern part of TG (Figure 1a). There, injection of water into the reservoir through the well Prati-9 started in November 2007. In April 2010, a second injection well (Prati-29) started also to inject water in the vicinity of the area of investigation. In this well, two trajectories were drilled, and it is unclear whether the fluid flows through both trajectories or along a preferential one. Until December 2011, no production occurred through the nearest producer well, Prati-25. A clear correlation between the monthly seismicity rate and the volume of water injected from both wells was observed (Figure 1b).

In the following analyses, we focused on the interpretation of time intervals framing the two injection cycles enclosing the most prominent peaks of fluid injection into the reservoir and inducing large number of seismic events. Seismicity from each cycle was divided into three subsets (stages) preceding, containing, and following the peak injection. Cycle 1 was composed of seismic activity framing the peak injection at well Prati-9, reaching a maximum flow rate of 0.24 Mm^3 per month. During Cycle 2, both wells Prati-9 and Prati-29 were active. Summing the injection volumes from both, a maximum injection rate of 0.32 Mm^3 per month was reached. Since water injection at TG follows a seasonal tendency, the peak injection usually occurred during the winter months. Note that the analyzed cycles do not contain any shut-in periods when the injection was stopped. The analyzed time intervals used in each stage are summarized in Table 1. The 1 year period between the two analyzed cycles was not further interpreted because there were not enough seismic events observed during this period to conduct reliable statistical analyses as described below.

Table 1. Time Intervals and Number of Events Used in Each Stage of the Analyzed Injection Cycles

	Stage	Time Interval	Number of Events
Cycle 1	Before	8 April to 8 September	24
	During	8 October to 9 February	59
	After	9 March to 9 September	30
Cycle 2	Before	10 June to 10 October	60
	During	10 November to 11 April	207
	After	11 May to 11 October	65

We initially used absolute hypocenter locations and focal mechanisms available from the catalogs of Northern California Earthquake Data Center (NCEDC). Approximately 1150 seismic events with moment magnitude M_w ranging between 1.0 and 3.3 were detected and located at the selected cluster of IS in the northwestern part of the field (Figure 1) during the time period between September 2007 and July 2012. Those hypocenters were determined using the HYPOINVERSE method [*Klein*, 2002] using a local 1-D gradient velocity model [*Eberhart-Phillips and Oppenheimer*, 1984]. To locate the events, seismic data from both local and regional stations were used. Given the good azimuthal coverage of the seismic network and the large number of stations, the reported average horizontal and vertical location uncertainty was in the order of 200 m and 300 m, respectively.

For the selected cluster of seismicity, 973 focal mechanisms were available in the NCEDC catalog during the analyzed time period. They were calculated with FPFIT [*Reasenberg and Oppenheimer*, 1985] software using on average more than 30 first-motion polarities per event. Daily injection rates were provided by Calpine Corporation.

We first investigated potential differences of the seismicity patterns during different stages of the injection cycle (before/during/after peak injections). As the original catalog did not display any particular spatial features (cf. Figure 1), we applied the double-difference earthquake relocation method to improve the precision of spatial offsets between the individual earthquake hypocenters [*Waldhauser and Ellsworth*, 2000]. The same velocity model as for the absolute location catalog was used. The double-difference method allowed improving the internal precision of the relative hypocentral locations down to 40 m. A total number of 770 events were successfully relocated. Our distribution of relocated hypocenters resolved the seismicity patterns similarly to the relocated catalog provided by *Waldhauser and Schaff* [2008].

Second, we recalculated the focal mechanisms with the FPFIT software based on the relocated hypocenter catalog and using all first-motion polarities available. The new focal mechanism catalog was categorized into strike-slip, normal, and thrust events based on the relative orientation of *P*/*T*/*B* axes (i.e., which of the axis was closer to the vertical).

We then traced the evolution of various kinematic, spatial, and source characteristics of IS with time to investigate their response to changes in injection rates:

1. Monthly distribution of the earthquake faulting types using all recalculated focal mechanisms.
2. Cumulative seismic moment release from the beginning of the analyzed period, separately for the three faulting types. The moment magnitude was recalculated from coda duration magnitude using the M_w-M_d relation estimated for TG [*Edwards and Douglas*, 2013] and converted to seismic moment using a standard relationship [*Hanks and Kanamori*, 1979].
3. Temporal evolution of the Gutenberg-Richter *b* values. This was calculated using the goodness of fit method [*Wiemer and Wyss*, 2000] for different moving time windows containing 55, 65, and 75 events, respectively. The values for the moving windows were selected to maximize the number of events at fixed resolution to visualize potential changes during peak injection intervals.
4. Temporal evolution of the relative stress magnitude $R = \frac{\sigma_1 - \sigma_2}{\sigma_1 - \sigma_3}$ from the stress inversion technique. The stress inversion was performed using the MSATSI package [*Martínez-Garzón et al.*, 2014], which is an updated version of SATSI [*Hardebeck and Michael*, 2006]. Stress inversion was performed using moving windows containing 55 events with a step size of 10. It should be noted that *R* is the parameter with the largest uncertainty for the stress inversion technique irrespective of the performed 95% confidence interval uncertainty assessment.
5. Temporal changes in the average hypocentral and epicentral distances of the seismicity from the bottom of the well Prati-9. The data were subdivided in moving windows as described for the stress inversion. Here we excluded those seismic events that seemed to be related to the injection into the nearby well (Prati-29, see Figure 2). The criteria to remove those events were based on time and proximity to the open hole from Prati-29 (see limiting line in Figure 2). Note that since a temporal criterion is also used, events close to Prati-29 might be included if they occurred before injection into the well started.
6. Evolution of the average static stress drop with time released by seismic events from different faulting types. The static stress drops were calculated following a slightly modified spectral fitting method [*Kwiatek et al.*, 2011, 2014]. The original three-component waveforms from stations located $<$20 km from the seismicity were initially filtered using a 1 Hz high-pass filter. Waveforms were analyzed with a window length of 0.40 s with additional 0.10 s period prior to either *P* or *S* wave onsets, respectively.

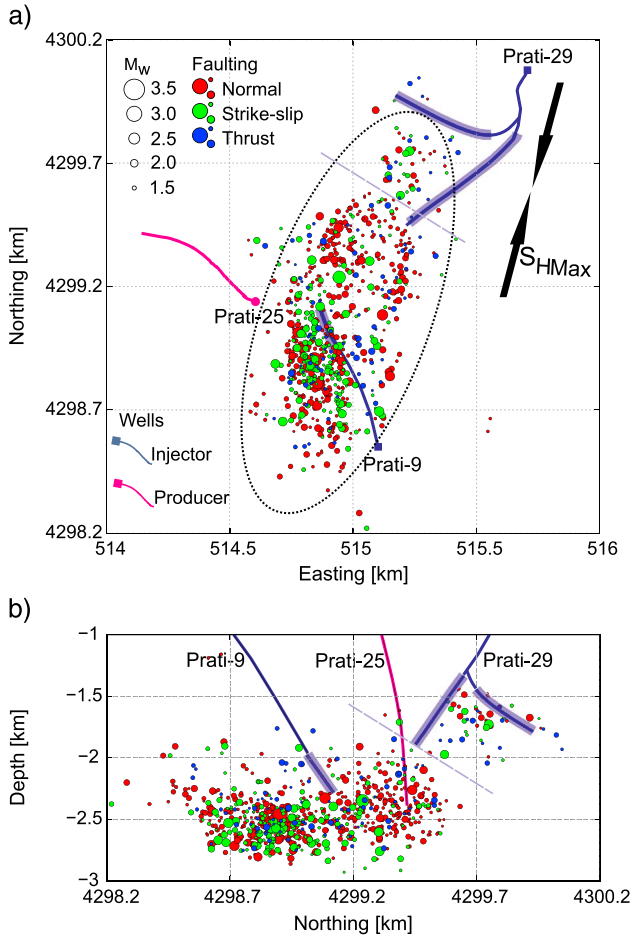

Figure 2. Relocated seismicity from the analyzed cluster at NW Geysers geothermal field. Violet dashed line separates earthquakes originating from injections into wells Prati-9 and Prati-29. Both traces drilled along Prati-29 are plotted. Semitransparent blue intervals mark the estimated open-hole sections. Easting and Northing coordinates are relative to the 10 S UTM zone. (a) Map view. (b) Depth section along the direction NS.

The windows were smoothed using von Hann's taper. Far-field ground velocity spectra $\dot{u}(f)$ were calculated from three-components of the sensor separately using the multitaper method [*Percival and Walden*, 1993] and then combined using $\dot{u}(f) = \left[\dot{u}_V(f)^2 + \dot{u}_{NS}(f)^2 + \dot{u}_{EW}(f)^2\right]^{0.5}$ [e.g., *Abercrombie*, 1995]. The observed ground velocity spectra were fitted using Boatwright's point-source model [*Boatwright*, 1978]:

$$\dot{u}(f; M_0, f_C, Q_C) = \frac{R_C}{2\rho V_C^3 R} \frac{f M_0}{\left(1 + (f/f_C)^4\right)^{0.5}} \exp\left(-\frac{\pi R f}{Q_C V_C}\right) \quad (1)$$

where R is the source-receiver distance, M_0 is the seismic moment, f_C is the corner frequency, Q_C is the quality factor, and R_C is the average radiation pattern correction coefficient of either P or S waves. Following *Boatwright and Boore* [1982], we used $R_P = 0.52$ and $R_S = 0.63$ for P and S waves, respectively. V_C stands for the P- or S- wave velocity in the source area. We assumed $V_P = 4100$ m/s and $V_S = 2441$ m/s using $V_P/V_S = 1.68$ [*Gritto and Jarpe*, 2014] and a density of $\rho = 2700$ kg/m^3. The logarithm of the modeled ground P and S velocity spectra described in equation (1) was fit to the observed spectra of P and S phases, and we inverted for (M_0, F_C, Q_C) separately for each station and phase. The optimization was performed using a grid-search technique followed by simplex refinement [cf. *Kwiatek et al.*, 2011, 2014]. The seismic moment was calculated from P and S phases as a median value from all stations fulfilling the quality criteria. The source radius was calculated in a similar way using corner frequencies of P waves and assuming the circular source model [*Madariaga*, 1976] with scaling constant $k = 2.01$

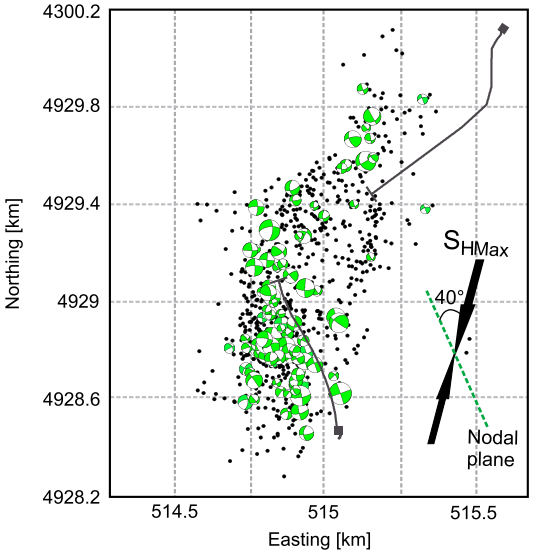

Figure 3. Map view of the focal mechanisms of the 100 strike-slip seismic events with the lowest focal mechanism solution misfit.

and a constant rupture velocity of $V_R = 0.9V_S$. Finally, the static stress drop was calculated following Eshelby's formula [*Eshelby*, 1957]:

$$\Delta\sigma_D = \frac{7}{16} M_0 r_0^{-3} \quad (2)$$

4. Results

The relocated hypocenter catalog and corresponding fault plane solutions allow identifying distinct spatial and temporal patterns of the seismicity not visible in the original catalog (Figure 2). Seismic events form an ellipsoid located below the open-hole section of Prati-9. The long axis of the seismicity cluster is oriented NNE/SSW parallel to the orientation of S_{HMax}. There is a significantly smaller shallow subcluster of seismicity around the open-hole section of well Prati-29.

The most common faulting mechanism is normal faulting, while a substantial number of events also display strike-slip faulting. Many of the strike-slip events form an elongated but diffuse zone in the NNW-SSE direction with one of the nodal planes typically aligned in similar direction (Figure 3). The existence of this NNW-SSE trending alignment of strike-slip faulting events (and one of their nodal planes) suggests the reactivation of a potential fault or a network of small faults at the base of the field that was previously unknown. The alignment of the strike-slip events and inferred fault(s) forms an angle of ~40° with respect to the orientation of S_{HMax}.

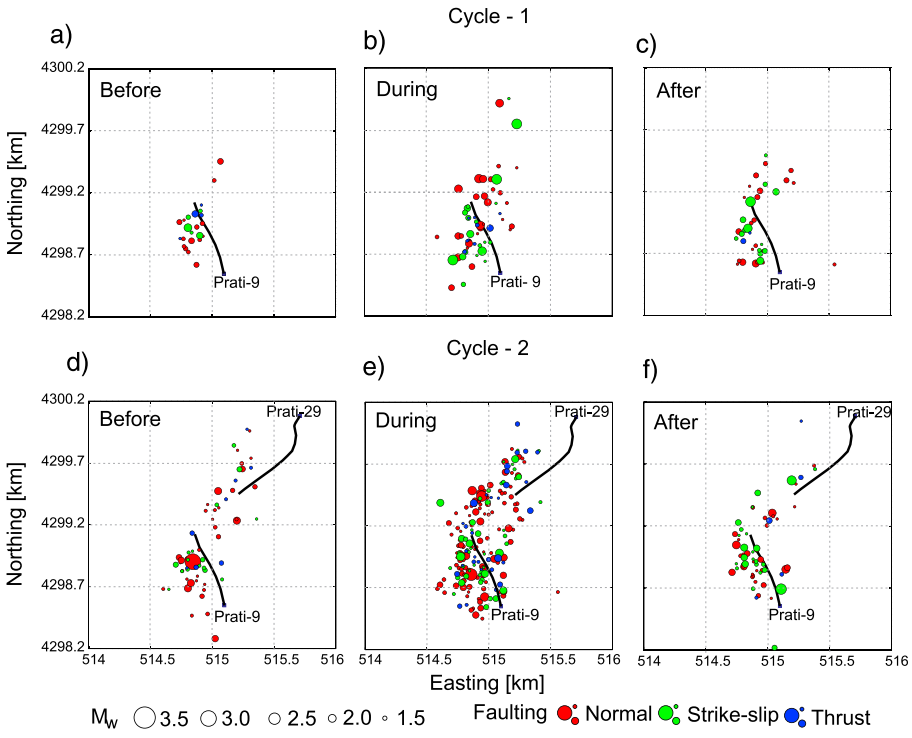

Figure 4. Snapshots of the spatial distribution of the seismicity during the different stages of both analyzed injection cycles. Symbol size represents the magnitude and symbol color represents the faulting style.

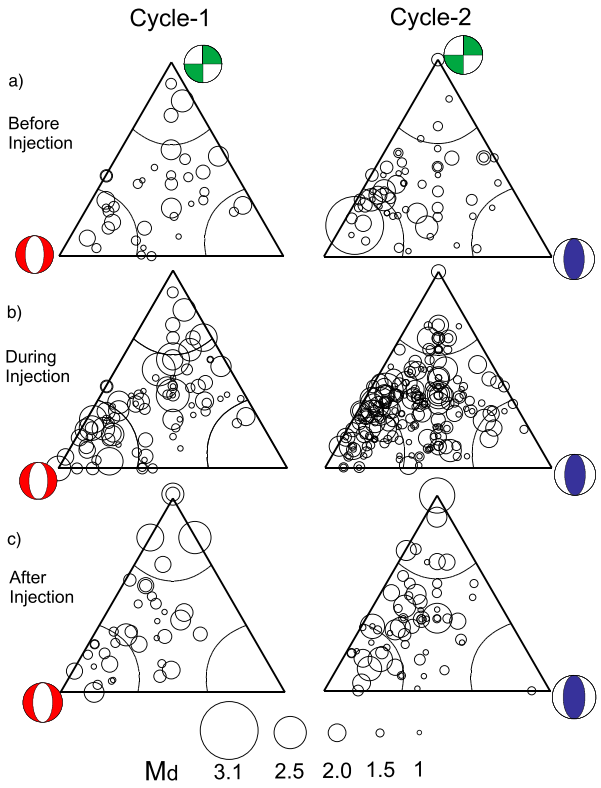

Figure 5. Ternary diagrams [*Frohlich*, 1991] for each of the stages of both analyzed injection cycles. Symbol size is scaled by with magnitudes. The angular lines mark 50° dip. Green: strike slip, red: normal faulting, and blue: thrust faulting.

Many normal faulting events are also located within this alignment, including the largest event from the analyzed cluster (M_w 3.3). Thrust events are sparse and evenly distributed throughout the whole cloud of IS.

In the following, we focus on potential variations of faulting kinematics and source parameters in relation to peak injections during both injection cycles. The spatial distribution of the seismicity before, during, and after peak injections reveals a distinct temporal evolution (Figure 4). For Cycle 1 (Figures 4a–4c), prior to and after the peak injection the seismicity was located mainly toward the south of the open-hole section of Prati-9 around the mentioned NNW-SSE alignment. In contrast, during the peak injection we observe a significant increase in seismic events extending NNE and SSW from the injection point, aligned with the orientation of S_{HMax} [*Oppenheimer*, 1986; *Provost and Houston*, 2003]. Spatial evolution of seismicity during Cycle 2 follows an analogous behavior, although some seismicity also occurs close to the injection well Prati-29. For both injection cycles, we also observe that some of the larger strike-slip events occur at a greater distance from the injection point during the peak injection, especially during Cycle 1.

The diversity of the fault plane solutions is displayed in Figure 5 showing ternary Frohlich diagrams plotted for each stage [*Frohlich*, 1991; *Bohnhoff et al*., 2004]. The dominant faulting style is normal faulting, in accordance with the local stress field [*Boyle and Zoback*, 2014]. However, a substantial part of the calculated focal mechanisms display mixed mode faulting. In particular, many events with mixed normal/strike-slip faulting behavior are observed, especially during peak injections. Note that many of the largest events from the analyzed cluster display pure strike-slip or very large strike-slip components. Especially for Cycle 2, many of the normal faulting events have small magnitudes ($M_d \sim 1$). During peak injections, the number of pure strike-slip (with some thrust faulting) events also increases. On average Cycle 1 displays fewer events than Cycle 2 but with larger magnitudes. Cycle 2 contains a larger amount of smaller events with a mixed normal/strike-slip faulting style. However, during the peak injection of Cycle 1, a larger number of small events were excluded in the relocation process.

For both original and relocated catalogs, the total number of seismic events per month is well-correlated with the injection rates (Figures 6a–6b). The number of events from each faulting type during different injection stages is summarized in Table 2. During high injection rates an increase in the number of normal faulting events is observed (Figure 6b). The number of strike-slip and thrust events also increases, but to a lesser extent. Interestingly, the percentage of normal faulting events is decreasing by approximately 20% at the time of peak injections. In consequence, the percentage of strike-slip and/or thrust faulting increases (Figure 6b). Still, particularly for Cycle 1, the number of relocated events is small and this might weaken the performed statistic on these events. During Cycle 2, the number of thrust faulting events and strike-slip events increased in similar proportion. However, during Cycle 1, the increase in strike-slip events is larger than the number of thrust events.

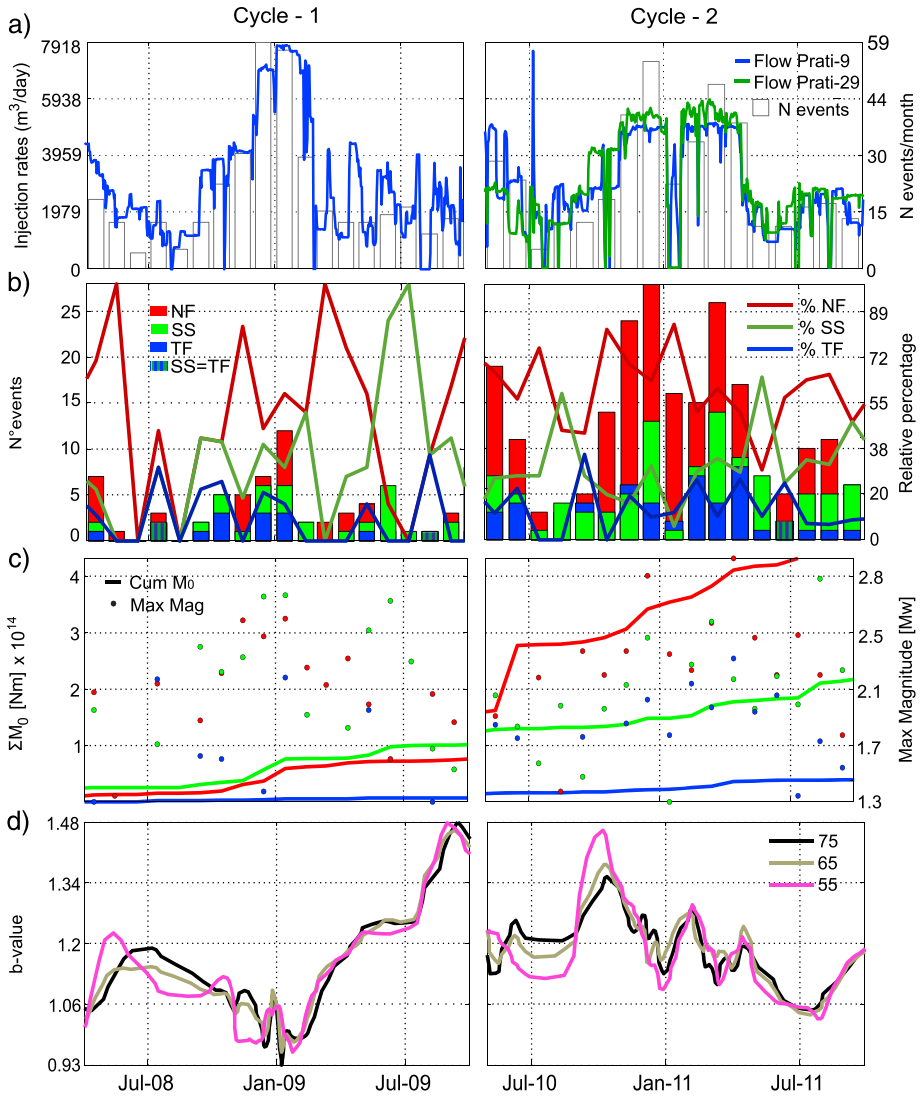

Figure 6. Temporal evolution of injection rates and seismic characteristics (Part II). Cycle 1 and Cycle 2. (a) Daily injection rates from Prati-9 and Prati-29 and monthly seismicity rate (original catalog). (b) Monthly number of events of each faulting type and percentage of each faulting style (relocated catalog). NF: normal faulting, SS: strike slip, and TF: thrust faulting. (c) Cumulative seismic moment (solid lines) and monthly maximum magnitude (dots) for each faulting type. Color is encoded as in Figure 6b). (d) *b* values for moving windows with a specific number of events.

The cumulative seismic moment released by normal faulting and strike-slip events increased during peak injections (Figure 6c). This is mainly due to the larger maximum magnitudes observed for the normal and strike-slip events at these injection stages (see maximum magnitudes in Figure 6c) and less importantly, to the larger number of seismic events at these times. In July 2010 the seismic moment release by normal faulting events reaches a maximum, mainly because of a single M_w 3.3 normal faulting event which occurred two months after injection started at Prati-29.

During both analyzed injection cycles, a short-term *b* value decrease is observed coinciding with peak injections (Figure 6d). In addition, a general trend toward decreasing *b* values is observed for Cycle 2. This trend is robust and independent of the size of the moving windows utilized to estimate the *b* value.

We also study variations of the relative stress magnitude *R* (*R* value) with time and injection history. Overall, the variations in the *R* value show some correlation with the injection rates and reflect a changing stress state in the reservoir when increased volumes of water are injected. During peak injection intervals, the relative stress magnitude increased slightly (Figure 7b). Although these changes are within statistical uncertainties,

Table 2. Number of Events From Each Faulting Style During Each Injection Stage

	Stage	Normal	Strike Slip	Thrust
Cycle 1	Before	10	6	4
	During	30	20	9
	After	15	13	2
Cycle 2	Before	36	16	8
	During	126	50	31
	After	35	25	5

they do correlate well with observed changes in principal stress orientation [*Martínez-Garzón et al.*, 2013]. Additionally, the average *R* value for the Cycle 1 (0.65) is higher than the average value for Cycle 2 (0.3). Thus, a steady decrease of *R* is observed between the two injection cycles. The average hypocentral and epicentral distances between the seismic events and the injection well Prati-9 also increase during peak injections (Figure 7c), particularly during Cycle 1 (Table 3).

During the first peak injection (Cycle 1), we observe a decrease in the average static stress drop of normal faulting events, and a slight increase in the stress drops of strike-slip events. (Figure 7d). The average static stress drop from thrust faulting events remains almost constant during Cycle 1. In contrast, during Cycle 2 no significant change in the average stress drop for any fault mechanism is observed.

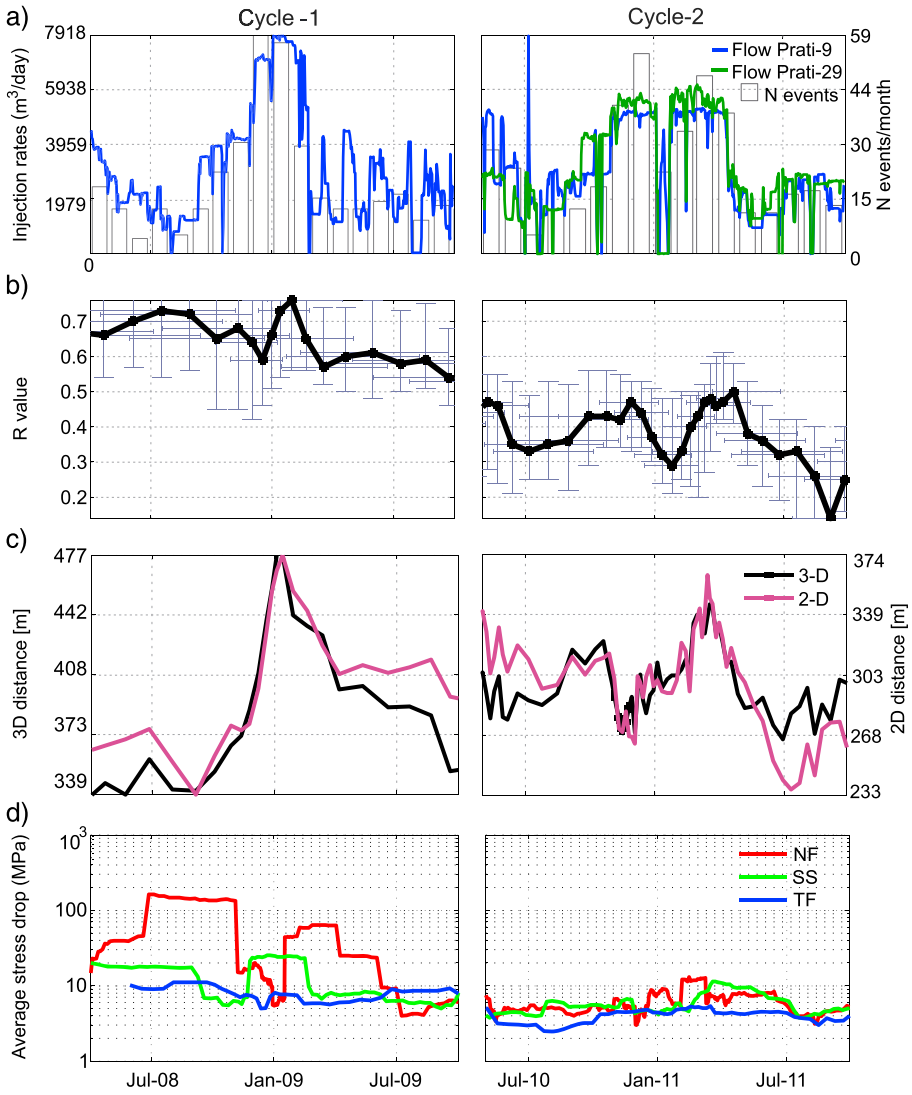

Figure 7. Temporal evolution of injection rates and seismic characteristics (Part II). Cycle 1 and Cycle 2. (a) Daily injection rates from Prati-9 and Prati-29 and monthly seismicity rate (original catalog). (b) Relative stress magnitude *R* (black line). Vertical lines represent 95% confidence intervals. (c) Hypocentral and epicentral distances from the well Prati-9. (d) Time evolution of average static stress drop from each faulting style. NF: normal faulting, SS: strike slip, and TF: thrust faulting.

Table 3. Average Hypocentral and Epicentral Distances Measured From the Bottom of the Well Prati-9 for Each Stage and Cycle

	Stage	3-D Distance (m)	2-D Distance (m)
Cycle 1	Before	339	233
	During	477	374
	After	408	260
Cycle 2	Before	400	300
	During	450	360
	After	370	235

5. Discussion

Analysis of the seismicity cluster in the NW Geysers geothermal field provides an excellent opportunity to gain additional insight in the mechanics governing IS associated with fluid injection. This relatively isolated seismicity cluster is especially interesting given the long injection history that includes several different injection cycles, abundant seismic activity, and a clear correlation between the injection rates and induced seismicity.

Recently, significant changes were observed in the stress field orientation during peaks of fluid injection into the reservoir [*Martínez-Garzón et al*., 2013]. The current study aims to understand the physical mechanisms governing the perturbation of the local stress field and the resulting changes in seismic response. The stress rotations were slightly more pronounced for the first peak injection (Cycle 1) at Prati-9. The observed changes in seismicity parameters described in the previous section follow a similar trend, being generally stronger during Cycle 1 than during Cycle 2. This may be attributed to the fact that Cycle 1 was the first major injection in this area, while Cycle 2 occurred after several subsequent injection cycles. Other factors also might have played a role, e.g., the split of the injection volume into two wells (Prati-9 and Prati-29).

5.1. Thermoelastic Versus Poroelastic Stress Perturbations

A potential explanation for observed temporal and spatial changes of the seismic characteristics during peak injection intervals may include an interplay of different physical mechanisms inducing seismicity. *Rutqvist et al*. [2013] recently suggested that thermal effects related to the injection of relatively cool water into the hot reservoir at depth may result in seismicity during the entire injection cycle (i.e., before/during/after peak injections). Thermoelastic stress perturbation is expected to promote fracturing and increase the permeability of reservoir rocks, given that a network of secondary cracks oriented perpendicular to the main fracture direction is introduced [*Ghassemi*, 2012]. Therefore, abundant microseismicity is likely to be observed in response to thermal contraction close to the well where cool surface water is injected (Figure 8). If the heat is transferred dominantly by conduction, no preferential direction is expected in the development of the seismic cloud induced by thermal fracturing. In contrast, if the heat transport was also assisted by advection of the relative hot pore fluid, anisotropy on the microseismicity distribution around the well may occur caused by preferential orientation of conductive fractures.

In addition, an injection-related increase in reservoir pore pressure may reactivate favorably oriented fractures within an existing network during peak injection periods. At TG, porosity of the rock matrix is only few percent, which suggests that fluid transport dominantly occurs along larger fractures rather than by flow through the matrix. However, at the spatial scale of interest in our study (few kilometers), it is expected that a large population of fractures exist at various length scales and orientation which allows us to view the reservoir effectively as a porous medium. Considering a laterally infinite, isotropic, porous, and linearly elastic reservoir that deforms uniaxially in the vertical direction, the change in horizontal stresses from fluid pressure change under constant vertical stress may be expressed as [see *Brown et al*., 1994]:

$$\Delta S_{H\mathrm{Max},h\mathrm{min}} = \alpha \frac{1-2\nu}{1-\nu}\Delta p, \tag{3}$$

where $S_{\mathrm{HMax},h\ \mathrm{min}}$ and S_V are the horizontal and vertical stresses at reservoir depth, respectively, ν is Poisson's ratio, and α is Biot's coefficient. Poroelastic changes of the reservoir stress state are often claimed to cause faulting, fracturing, and even changes in the stress regime resulting from production activities in hydrocarbon and geothermal reservoirs [*Segall et al*., 1994; *Altmann et al*., 2014].

Thermal and pore pressure effects may operate concurrently at different temporal and length scales depending on the diffusivity of heat and pore pressure, which are governed by the thermal and transport properties of the reservoir. Below, we estimate the relative contributions of pore pressure and thermal effects during injection on the prevailing stress field and their respective roles for inducing faulting and seismicity (Figure 8).

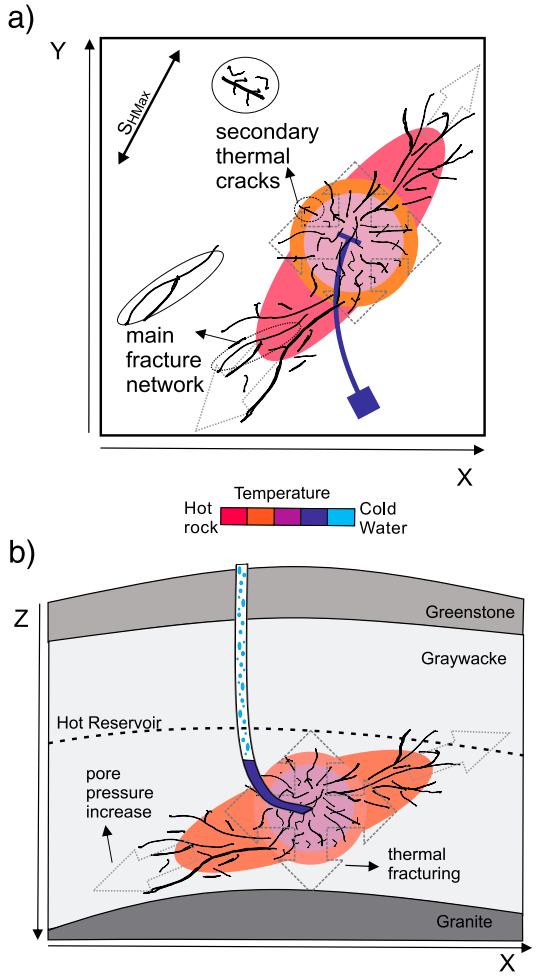

Figure 8. Schematic diagram depicting physical mechanisms responsible for IS at the selected cluster of seismicity from The Geysers. (a) Map view and (b) depth view. Thermoelastic effect occurs near the injection well. The thermoelastic stress perturbation is initially assumed to result from isotropic heat conduction, and it may appear ellipsoidal if heat is transported by advection through an anisotropic fracture network (see text for details). The pore pressure diffuses further from the well through the main fracture network aligned with S_{HMax}.

Thermal fracturing caused by relatively cool fluid injection is assumed to be the primary cause responsible for IS at TG based on a series of modeling studies and research conducted by the field operator (Calpine Corporation) [e.g., *Majer et al.*, 2007; *Rutqvist et al.*, 2013]. In the northwestern part of TG, relatively cool water at approximately surface temperature (≈20–25°C) is injected into the reservoir. According to a pressure-temperature log performed in the well Prati-9 in December 2011, the water temperature at the bottom of the well was approximately 76°C. The injected water is heated rapidly by the surrounding rocks of the reservoir (240°C at the well Prati-9) [*García et al.*, 2012]. Considering these temperatures, the thermally induced changes in the circumferential stress $\Delta\sigma_T$ directly at the wellbore may be estimated using [*Stephens and Voight*, 1982]:

$$\Delta\sigma_T = -\frac{\alpha_L E \Delta T}{1-\nu}, \tag{4}$$

where α_L is the coefficient of linear thermal expansion of the reservoir rock, E is the Young modulus of the reservoir rock, ΔT is the difference in temperature between the reservoir rock and the water, and ν is the Poisson's ratio. If we assume $\alpha_L = 1 \cdot 10^{-5} K^{-1}$ [*Segall and Fitzgerald*, 1998], $E = 12 \cdot 10^9$ Pa, $\nu = 0.25$, and the above temperatures difference, we estimate a thermally induced tensile stress magnitude of approximately −26 MPa from strong thermal contraction at the wellbore wall, although the induced stress changes attenuate very rapidly with distance. Also, at the depth of the seismicity cluster studied here, the temperature is expected to increase strongly with depth, reaching 340°C only a few hundred meters deeper. Therefore, our estimate of the thermal stress induced at the borehole is considered conservative.

At TG, the pore pressure at reservoir depth is subhydrostatic. The height of the water column filled inside the well remains mostly within the reservoir limits, (<1 km from the bottom of the well). However, the increase in the injection rate closely correlates with migration of IS suggesting that pore pressure changes may also influence seismic activity (Figure 1b). Also, the spatial extent of the seismic cloud suggests that seismicity is induced by pore pressure changes at larger distance to the well.

We estimate the pore pressure at the Prati-9 injection well by analyzing the pressure record observed during an injectivity test conducted in December 2011. During this test, sustained injection rates of 2725 m^3/d (representative for the time periods before and after peak injections), 4933 m^3/d, and 8231 m^3/d (representative for peak injections) resulted in pressures of approximately 2.75 MPa, 3.17 MPa, and 3.79 MPa, respectively, for a tool suspended at a measured depth of 2682 m. With a total measured depth of 3053 m for Prati-9, this indicates total water column heights of approximately 668 m at 2725 m^3/d, 712 m at 4933 m^3/d, and 779 m at 8231 m^3/d and corresponding total bottomhole pressures of approximately 6.20 MPa, 6.60 MPa, and 7.23 MPa, respectively.

In this calculation, only the fluid injected into the well Prati-9 is taken into account. The obtained pore pressures always remain subhydrostatic and a pore pressure difference of about 1 MPa is estimated between peak injection and pre/post injection periods. This value is still relevant considering the minimum necessary pore pressures estimated to induce seismicity, which may be significantly smaller [*Rothert and Shapiro*, 2007]. A maximum pore pressure of 7.23 MPa was estimated during December 2008 to Jan 2009 based on the injection rates from this well. During Cycle 2, fluid was also injected from the well Prati-29, and therefore, estimating the pore pressure is more difficult than for Cycle 1. However, total injection rate was higher in Cycle 2 so that we can expect a pore pressure perturbation of approximately the same order.

The relation between the three injection rates and bottom hole pressure values recovered from the injectivity test is almost linear and yields an injectivity index I of about 6.16×10^{-12} m^3/s/MPa. By approximating that water is injected radially from a vertical well into a reservoir with infinite horizontal extent, we estimate the reservoir permeability k from the injectivity index using an equation based on the Theis solution [*Theis*, 1935] that relates the spatial and temporal evolution of pore pressure with the flow rate at the well:

$$k = -\frac{I\eta}{4\pi h}\,\mathrm{Ei}\left(\frac{-\eta\phi c_w d^2}{4kt}\right) \qquad \text{where } \mathrm{Ei}(x) = \int_{-\infty}^{x}\frac{e^{x'}}{x'}\mathrm{d}x' \tag{5}$$

Here η is pore fluid viscosity, h is the reservoir height, ϕ is the porosity of the formation, c_w is the compressibility of water, d is the well diameter, t is the time span of the fluid flow since the beginning of injection, and Ei(x) is the exponential integral function. For physical property values estimated for a representative reservoir condition of 150°C and 5 MPa pore pressure (Table 4), equation (5) yields reservoir permeability of about 1.3×10^{-14} m^2. Note that we assigned t as 1 h although pressure readings at different injection rates were obtained at different times after the start of the injectivity test between 0.5 and 3 h. However, the change in estimated permeability is less than 10% whether t is taken as 0.5 or 3 h.

Both temperature and pore pressure perturbations diffuse into the reservoir from the injection well governed by the diffusion equation with some characteristic diffusivity that determines the spatial extent to which these perturbations reach from the injection well at a given time. These diffusivities are the thermal diffusivity, $K_{\mathrm{thermal}} = {}^{\kappa}/_{\rho c_h}$, and the hydraulic diffusivity, $K_{\mathrm{hydraulic}} = {}^{k}/_{\phi\eta c_w}$, for temperature and pore pressure changes, respectively. Based on the hydraulic properties calculated above and thermal properties from the literature (Table 4), we estimate that K_{thermal} is on the order of 10^{-6} m^2/s, whereas $K_{\mathrm{hydraulic}}$ is of the order of 10^{1} m^2/s. Because diffusion length scales with the square root of the diffusivity constant, these calculations suggest that there is at least 3 orders of magnitude difference in the distance to which pore pressure changes induce poroelastic stress perturbations compared to thermal elastic stress changes assuming heat is only transported by thermal conduction.

Temperature anomalies may also be transported by advection of the injected fluid. For instance, we consider the radial distance the injected water travels from the injection well assuming radial injection into a cylindrical reservoir volume with 1000 m reservoir thickness and 2% reservoir porosity (Table 4). Since the beginning of the water injection in November 2007 to December 2011, there had been approximately 5 Mm^3 of water injected from Prati-9 into this reservoir. Assuming the geometries given above, this suggests that the injected water would have reached a distance of about 280 m away from the well. On the other hand, the hydraulic diffusion length ($D_{\mathrm{hydraulic}}$) for 1 month time estimated from the hydraulic diffusivity ($D_{\mathrm{hydraulic}} = (K_{\mathrm{hydraulic}}\cdot t)^{1/2}$) is on the order of 10^3 m. Therefore, even if advection was the dominant mechanism for heat transport during the injection, we expect that the spatial extent to which poroelastic mechanisms induce seismicity is much larger than the spatial extent of IS caused by thermoelastic stresses.

These two mechanisms to induce seismicity affect differently the distribution of principal stresses in the reservoir. In a similar way to reservoir depletion [*Segall and Fitzgerald*, 1998], volumetric contraction of the reservoir rock due to cooling should reduce the horizontal stresses at least locally. This can be illustrated schematically in a Mohr circle diagram (Figure 9). Assuming a normal faulting stress regime, a reduction of the intermediate and minimum stress would result in a larger differential stress and a stress state closer to the failure envelope (Figure 9a). In contrast, as a consequence of the pore pressure increase, the three effective principal stresses should decrease and the Mohr circle would be shifted toward the failure envelope (Figure 9b). This effect alone would not create a rotation of the stress tensor that was observed previously [*Martínez-Garzón et al*., 2013]. Simultaneously, an increase in the pore pressure also increases the absolute

Table 4. Physical Properties and Reservoir Parameters Used for Estimation of Diffusivities

Property	Given Value	Reference
Water dynamic viscosity, η	0.171	*Batzle and Wang* [1992]
Porosity, ϕ	2%	*Barker et al.* [1992]
Water compressibility, c_w	5. 10^{-4} MPa	*Batzle and Wang* [1992]
Reservoir height, h	1000 m	Calpine Corporation
Borehole radius, r	10.80 cm	Calpine Corporation
Time span (during injectivity test), t	1 h	
Rock density, ρ	2700 kg/m^3	
Thermal conductivity, κ	3.2 W/m/°C	*Rutqvist et al.* [2013]
Specific heat capacity, c_h	1000 J/kg/°C	*Rutqvist et al.* [2013]

value of the horizontal stresses (equation (3)). The combined effect of both poroelastic stress and pore pressure changes from fluid injection result in shifting the Mohr circle toward the failure criteria. Assuming isotropic expansion of the pore pressure away from the well, radial horizontal effective stress components will experience less reduction than the tangential horizontal effective stress components [*Altmann et al.*, 2014]. In a normal faulting environment, this results in larger differential stresses along the S_{HMax} direction [*Schoenball et al.*, 2010; *Altmann et al.*, 2014] promoting preferentially oriented shear failure and seismic activity.

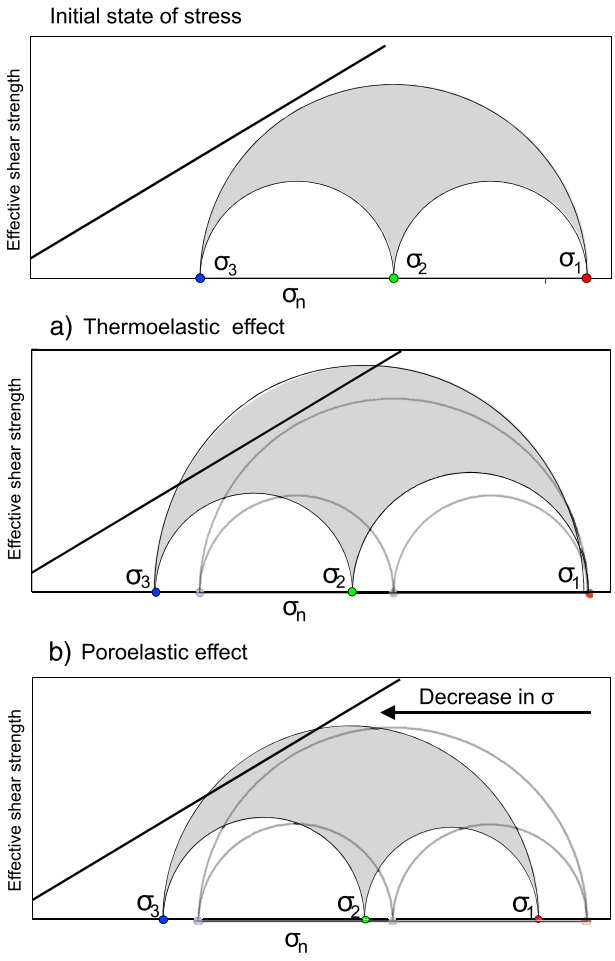

Figure 9. Conceptual illustration of the variation of the principal stresses on the Mohr circle. Normal faulting is assumed. (a) Changes in differential and mean stress due to the thermoelastic effects. (b) Changes in circle differential and mean stress from poroelastic effects (see text for details).

The conclusions of this study using observed seismicity are in general agreement with geomechanical modeling of an Enhanced Geothermal System (EGS) system located approximately 1 km to the west [*Rutqvist et al.*, 2013]. The authors concluded that the EGS-induced seismicity was primarily due to thermal contraction, with a secondary contribution from reservoir steam pressure changes.

In our study, the influence of reservoir depletion is not considered because no production was being performed during the analyzed times in the area. However, reservoir depletion is also expected to affect the seismicity at TG on larger time and spatial scales.

5.2. Hypocenter Distribution and Faulting Mechanism

The spatial pattern of relocated seismicity (Figures 2 and 4) reflects the regional stress field in that the first-order ellipsoidal shape of the seismic cloud has the long axis subparallel to S_{HMax}. This orientation is consistent with both the regional stress field and with the direction of preferred fault planes studied in a seismicity cluster nearby [*Boyle and Zoback*, 2014]. This suggests that the regional stress field generally dominates the spatial distribution of the IS during the analyzed time period. The

alignment of seismicity with S_{HMax} has also been observed in other geothermal projects, as in Soultz-sous-Forêts [*Cuenot et al*., 2006; *Cornet et al*., 2007]. For Soultz-sous-Forêts, it has been suggested that the elongated shape of the seismic cloud may be related to activation of a fault network and fluid pathways preferentially aligned parallel to S_{HMax}. Alternatively, numerical modeling of poroelastic stress changes from fluid injection indicates increased differential stresses promoting failure dominantly parallel to the S_{HMax} direction [*Schoenball et al*., 2010]. Both effects may be responsible for the observed ellipsoidal shape of the seismicity cluster.

It has been suggested previously that the migration of IS triggering front away from the injection well is controlled by hydraulic diffusion in the reservoir [*Shapiro et al*., 2002]. The gradual evolution of the triggering front with time after shut-in has been observed in several field studies [*Shapiro et al*., 2002; *Bachmann et al*., 2011; *Albaric et al*., 2014]. However, here we observe a short-term correlation between ongoing fluid injection and the occurrence of seismicity at some distance to the well that was not previously noted. Note also that the seismicity collapses toward the injection point once the flow rate of the injected water has decreased (pulsation of the seismic cloud). This behavior is conceptually different from that of the back front of the seismicity as described by *Parotidis et al*. [2004]. These authors stated that no seismic event is expected to occur close to the injection point once the injection has stopped. In this study, we are not expecting to observe a back-front since there is no shut-in. Our observations are in better agreement with an almost instantaneous or at least rapid poroelastic perturbation of the stress field caused by the injection.

5.3. *b* Values and Static Stress Drop

The observed decrease in *b* values during peak injections may be interpreted as the result of increased contribution by strike-slip and thrust faulting events with larger magnitudes on average. Analyzing seismic catalogs of California and Japan, *Schorlemmer et al*. [2005] observed that *b* values depend on faulting regime, with the largest *b* values found for normal faulting, intermediate *b* values for strike-slip faulting, and the lowest *b* values for thrust faulting. Given that stresses in a thrust faulting regime are expected to be higher than in a normal faulting regime, the authors suggested that *b* values depend inversely to the differential stress and may be used as a stress meter. We find that during peak injection, the relative contribution of strike-slip and thrust faulting events slightly increases and simultaneously *b* values decrease. This may suggest that during peak injection and along the maximum stress direction, horizontal stresses increased as predicted by numerical modeling [*Schoenball et al*., 2010]. Our findings cannot be directly compared to the results found for the Basel Deep Heat Mining Project, where a decrease in the *b* values occurred between the injection period and the postinjection period [*Bachmann et al*., 2011]. Note that there are some differences between the Basel Deep Heat Mining Project (or the EGS at Soultz-sous-Forêts) and our case study at The Geysers, the most important ones being the lower pore pressure at the reservoir level and the longer timescale of the injection at The Geysers. However, the physical mechanisms governing seismicity induced by fluid injection should be comparable. At TG, we also observe a change of the dominant faulting regime, which at the Basel site remains to be strike slip [*Terakawa et al*., 2012].

The observed small variations of the stress drop observed during Cycle 1 in the normal faulting and strike-slip events are not significant to allow for conclusions. Additionally, the fact that they only occur during Cycle 1 complicates their interpretation. Results showing that the stress drop associated with thrust faulting is larger than that associated with normal faulting have been reported for a number of previous studies [e.g., *Cocco and Rovelli*, 1989; *McGarr and Fletcher*, 2002], but it is not always seen.

5.4. Stress Magnitudes

To estimate effective stress magnitudes at reservoir depth, we used the calculated pore pressures and information from a density log (available online at the Department of Conservation State of California). Assuming an average density of the greywacke reservoir rock $\rho_g = 2700\,\mathrm{kg/m^3}$, the vertical stress is calculated from

$$S_V = \rho_g g z \tag{6}$$

where g is the gravitational acceleration and z is the average depth. For an average depth of 2.4 km for the analyzed seismicity, taking into account the elevation of the well Prati-9 (663 m) and assuming a normal faulting stress regime, a value of $S_V = S_1 = 78$ MPa is obtained.

We assume that maximum stresses in the reservoir are limited by critically stressed faults that are close to failure. This is supported by the observation of IS occurring with small pore pressure perturbations (~1 MPa). For frictional equilibrium of optimally oriented faults the ratio between maximum and minimum effective stress assuming normal faulting stress regime is limited by [*Jaeger and Cook*, 1971]:

$$\frac{S_V - p}{S_{h\min} - p} = \left[\sqrt{\mu^2 + 1} + \mu\right]^2 \tag{7}$$

where μ is the friction coefficient. Assuming a value of $\mu = 0.85$ [*Byerlee*, 1978], and a minimum pore pressure of $p = 6$ MPa for the periods before and after peak injections, we estimate a lower boundary for the minimum horizontal stress $S_{h\min} = 21$ MPa for the time period before the peak injection.

To estimate a corresponding lower boundary for the intermediate stress, S_{HMax}, we use the relative stress magnitude R estimated from stress inversion. A representative R value for Cycle 1 is $R = 0.65$ and the intermediate stress can be estimated from

$$R = \frac{\sigma_1 - \sigma_2}{\sigma_1 - \sigma_3}. \tag{8}$$

The resulting intermediate stress is $S_{\mathrm{HMax}} = 41$ MPa before peak injection. Therefore, the initial effective stress magnitudes for the time period before the peak injection (assuming a pore pressure of 6 MPa) would be about $\sigma_V = 72$ MPa, $\sigma_{\mathrm{HMax}} = 35$ MPa, $\sigma_{h\min} = 15$ MPa.

During the first peak injection, the pore pressure increases approximately $\Delta p = 1$ MPa with respect to the previous injection stage. Additionally, the horizontal stresses in radial direction from the injection well will increase during the peak injection according to equation (3). Assuming a Poisson's ratio of $\nu = 0.25$ and a maximum Biot coefficient of $\alpha = 1$, we obtain a maximum increase of the horizontal stresses of $\Delta S_{\mathrm{HMax},\ h\min} = 0.7$ MPa.

Note that, by taking into account the value of the thermal stresses estimated at the wellbore, the effective stresses in direct proximity to the wellbore wall are reduced such that $\sigma_{h\min}$ would exceed reported tensile strength for greywacke sandstone (8–12 MPa) [*Holub et al.*, 2009], although the spatial extent of the thermoelastic stresses is time dependent and it would be hard to quantify.

6. Conclusions

In this study, we analyzed spatiotemporal changes, faulting regimes, and source parameters of induced seismicity associated with two fluid injection cycles performed in the northwestern part of The Geysers geothermal field, California. Both injection cycles included a peak injection interval and periods of moderate injection rates before and afterwards. We created an improved hypocenter catalog by relocating a total of 770 induced seismic events and also calculated their fault plane solutions.

From aligned strike-slip events we suggest the presence of a previously unknown local fault in the vicinity of this injection area, which is favorably oriented with respect to the regional stress field. Depending on the size of the fault, this observation may have further implications for the local seismic hazard.

The spatiotemporal distribution of the seismicity, faulting kinematics, *b* values, relative stress magnitude and distance from the injection well all show substantial changes during the times of peak-fluid injection with respect to the times before and afterward. Most of these quantities reflect the change in the reservoir state of stress during periods of enhanced injection rates, in agreement with previously observed changes in the stress field orientation during peaks of fluid injection. During the peak injection intervals the absolute number of normal faulting events increased but the relative number of strike-slip and thrust faulting events also increased slightly (~15%). A decrease in *b* values simultaneous with the increase in relative amount of strike-slip and thrust events at peak injection rates has been observed. Additionally, the average distance of the seismicity from the injection well is seen to increase significantly during the peak injections, suggesting a change in the spatial scale of the hypocenter cloud while the long axis of the ellipsoid is subparallel with S_{HMax}.

Our results suggest that fluid injection may induce thermoelastic and poroelastic effects that change the local stress field in a reservoir on different time and spatial scales. These local stress changes possibly govern IS

mainly by activating a network of critically stressed faults. At TG, the high reservoir temperature (>240°C) and the large temperature difference with the injected fluid induces high thermal stresses at the wellbore wall (~ − 26 MPa) that significantly exceed the induced difference in pore pressure $\Delta P = 1$ MPa. This suggests that near the well thermoelastic effects dominate over poroelastic stress changes regardless of the injection stage. However, at some distance to the well and during the peak-fluid injections, pore pressure diffusion likely dominates causing the observed seismicity as suggested by calculating characteristic length scales of thermal and pore pressure effects, regardless of the mechanisms for heat transport.

Acknowledgments

We acknowledge funding within the Helmholtz-Alberta Initiative and from the Helmholtz Association in the framework of the Young Investigators Group "From microseismicity to large earthquakes." We thank the Northern California Earthquake Data Center (NCEDC), Lawrence Berkeley National Laboratory, and David Oppenheimer for providing the seismic data catalogs. We thank Calpine Corporation for high-resolution hydraulic data and additional relevant information related to The Geysers geothermal field. We thank Luca Urpi for early discussions and Martin Schoenball for providing a ternary plot code. We finally thank the reviewers Martin Schoenball and Danielle Sumy for many useful comments that substantially improved the manuscript.

References

Abercrombie, R. E. (1995), Earthquake source scaling relationships from −1 to 5 M_L using seismograms recorded at 2.5-km depth, *J. Geophys. Res.*, *100*, 24,015–24,036, doi:10.1029/95JB02397.

Albaric, J., V. Oye, N. Langet, M. Hasting, I. Lecomte, K. Iranpour, M. Messeiller, and P. Reid (2014), Monitoring of induced seismicity during the first geothermal reservoir stimulation at Paralana, Australia, *Geothermics*, doi:10.1016/j.geothermics.2013.10.013.

Allis, R. G. (1982), Mechanism of induced seismicity at The Geysers Geothermal Reservoir, California, *Geophys. Res. Lett.*, *9*, 629–632, doi:10.1029/GL009i006p00629.

Altmann, J. B., O. Heidbach, and R. Gritto (2013), Relative importance of processes leading to stress changes in The Geysers Geothermal area, in *Proceedings of the Thirty-Eight Workshop on Geothermal Reservoir Engineering*, Stanford Univ., Stanford, Calif., 11–13 Feb., SGP-TR-198. [Available at https://pangea.stanford.edu/ERE/db/IGAstandard/record_detail.php?id=18981.]

Altmann, J. B., B. I. R. Müller, T. M. Müller, O. Heidbach, M. R. P. Tingay, and A. Weißhardt (2014), Pore pressure stress coupling in 3D and consequences for reservoir stress states and fault reactivation, *Geothermics*, doi:10.1016/j.geothermics.2014.01.004.

Bachmann, C. E., S. Wiemer, J. Woessner, and S. Hainzl (2011), Statistical analysis of the induced Basel 2006 earthquake sequence: Introducing a probability-based monitoring approach for Enhanced Geothermal Systems, *Geophys. J. Int.*, *186*(2), 793–807, doi:10.1111/j.1365-246X.2011.05068.x.

Bachmann, C. E., S. Wiemer, B. P. Goertz-Allmann, and J. Woessner (2012), Influence of pore-pressure on the event-size distribution of induced earthquakes, *Geophys. Res. Lett.*, *39*, L09302, doi:10.1029/2012GL051480.

Barker, B. J., M. S. Gulati, M. A. Bryan, and K. L. Reidel (1992), Geysers reservoir performance, *Monogr. Geysers Geotherm. Field Spec. Rep.*, *17*, (Geothermal Research Council), 167–178.

Batzle, M., and Z. Wang (1992), Seismic properties of pore fluids, *Geophysics*, *57*(11), 1396–1408.

Boatwright, J. (1978), Detailed spectral analysis of two small New York State earthquakes, *Bull. Seismol. Soc. Am.*, *68*, 1131–1177.

Boatwright, J., and D. M. Boore (1982), Analysis of the ground accelerations radiated by the 1980 Livermore Valley earthquakes for directivity and dynamic source characteristics, *Bull. Seismol. Soc. Am.*, *72*(6A), 1843–1865.

Bohnhoff, M., S. Baisch, and H.-P. Harjes (2004), Fault mechanisms of induced seismicity at the superdeep German Continental Deep Drilling Program (KTB) borehole and their relation to fault structure and stress field, *J. Geophys. Res.*, *109*, B02309, doi:10.1029/2003JB002528.

Boyle, K., and M. Zoback (2014), The Stress State of the Northwest Geysers, California Geothermal Field, and Implications for Fault-Controlled Fluid Flow, *Bull. Seismol. Soc. Am.*, doi:10.1785/0120130284.

Brophy, P., M. J. Lippmann, P. F. Dobson, and B. Poux (2010), The Geysers geothermal field: Update 1990–2010, Geothermal Resour., Council, Spec. Rep.

Brown, K. M., B. Bekins, B. Clennell, D. Dewhurst, and G. Westbrook (1994), Heterogeneous hydrofracture development and accretionary fault dynamics, *Geology*, *22*(3), 259–262, doi:10.1130/0091-7613(1994)022<0259:HHDAAF>2.3.CO;2.

Byerlee, J. (1978), Friction of rocks, *Pure Appl. Geophys.*, *116*(4–5), 615–626, doi:10.1007/BF00876528.

Cocco, M., and A. Rovelli (1989), Evidence for the variation of stress drop between normal and thrust faulting earthquakes in Italy, *J. Geophys. Res.*, *94*, 9399–9416, doi:10.1029/JB094iB07p09399.

Cornet, F. H., T. Bérard, and S. Bourouis (2007), How close to failure is a granite rock mass at a 5 km depth?, *Int. J. Rock Mech. Min. Sci.*, *44*(1), 47–66, doi:10.1016/j.ijrmms.2006.04.008.

Cuenot, N., J. Charléty, L. Dorbath, and H. Haessler (2006), Faulting mechanisms and stress regime at the European HDR site of Soultz-sous-Forêts, France, *Geothermics*, *35*(5–6), 561–575, doi:10.1016/j.geothermics.2006.11.007.

DeCourten, F. (2008), Geology of Northern California, 48 pp. [Available at http://www.cengage.com/custom/regional_geology.bak/data/DeCourten_0495763829_LowRes_New.pdf.]

Dost, B., and H. K. Haak (2007), Natural and induced seismicity, in *Geology of the Netherlands*, edited by T. E. Wong, D. A. J. Batjes, and J. de Jager, pp. 223–239, Royal Netherlands Academy of Arts and Sciences, Amsterdam.

Eberhart-Phillips, D., and D. H. Oppenheimer (1984), Induced seismicity in The Geysers geothermal area, California, *J. Geophys. Res.*, *89*, 1191–1207, doi:10.1029/JB089iB02p01191.

Edwards, B., and J. Douglas (2013), Magnitude scaling of induced earthquakes, *Geothermics*, doi:10.1016/j.geothermics.2013.09.012.

Ellsworth, W. L. (2013), Injection-induced earthquakes, *Science*, *341*(6142), 1225942, doi:10.1126/science.1225942.

Eshelby, J. D. (1957), The determination of the elastic field of an ellipsoidal inclusion, and related problems, *Proc. R. Soc. London, Ser. A*, *241*(1226), 376–396, doi:10.1098/rspa.1957.0133.

Evans, K. F., A. Zappone, T. Kraft, N. Deichmann, and F. Moia (2012), A survey of the induced seismic responses to fluid injection in geothermal and CO_2 reservoirs in Europe, *Geothermics*, *41*, 30–54, doi:10.1016/j.geothermics.2011.08.002.

Foulger, G. R., C. C. Grant, A. Ross, and B. R. Julian (1997), Industrially induced changes in Earth structure at The Geysers Geothermal Area, California, *Geophys. Res. Lett.*, *24*, 135–137, doi:10.1029/96GL03152.

Frohlich, C. (1991), Display and quantitative assessment of distributions of earthquake focal mechanisms, *Geophys. J. Int.*, *144*, 300–308.

García, J., M. Walters, J. Beall, C. Hartline, A. Pingol, S. Pistone, and M. Wright (2012), Overview of the north-western Geysers EGS demonstration project, in *Proceedings Thirty-Seventh Workshop Geothermal Reservoir Engineering*, Stanford Univ., Stanford, Calif., 30 Jan.–1 Feb., SGP-TR-194.

Ghassemi, A. (2012), A review of some rock mechanics issues in geothermal reservoir development, *Geotech. Geol. Eng.*, *30*(3), 647–664, doi:10.1007/s10706-012-9508-3.

Goertz-Allmann, B. P., A. Goertz, and S. Wiemer (2011), Stress drop variations of induced earthquakes at the Basel geothermal site, *Geophys. Res. Lett.*, *38*, L09308, doi:10.1029/2011GL047498.

Gritto, R., and S. P. Jarpe (2014), Temporal variations of Vp/Vs-ratio at The Geysers geothermal field, USA, *Geothermics*, 1–8, doi:10.1016/j.geothermics.2014.01.012.

Gunasekera, R. C., G. R. Foulger, and B. R. Julian (2003), Reservoir depletion at The Geysers geothermal area, California, shown by four-dimensional seismic tomography, *J. Geophys. Res.*, *108*(B3), 2134, doi:10.1029/2001JB000638.

Hanks, T. C., and H. Kanamori (1979), A moment magnitude scale, *J. Geophys. Res.*, *84*, 2348–2350, doi:10.1029/JB084iB05p02348.

Hardebeck, J. L., and A. J. Michael (2006), Damped regional-scale stress inversions: Methodology and examples for southern California and the Coalinga aftershock sequence, *J. Geophys. Res.*, *111*, B11310, doi:10.1029/2005JB004144.

Holub, K., P. Konečný Jr., and J. Knejzlík (2009), Investigation of the mechanical and physical properties of greywacke specimens, *Int. J. Rock Mech. Min. Sci.*, *46*(1), 188–193, doi:10.1016/j.ijrmms.2008.02.011.

Hulen, J. B., J. C. Quick, and J. N. Moore (1997a), Converging evidence for fluid overpressures at peak temperatures in the pre-vapor dominated Geysers Hydrothermal system, *Geotherm. Reseour. Council Trans.*, *21*, 623–628.

Hulen, J. B., M. T. Heizler, J. A. Stimac, J. N. Moore, and J. C. Quick (1997b), *New Constraints on the Timing and Magmatism, Volcanism and the Onset of the Vapor Dominated Conditions at The Geysers Steam Field, California*, pp. 75–82, Stanford Univ., Stanford, Calif.

Jaeger, J., and N. G. Cook (1971), Fundamentals of Rock Mechanics.

Jeanne, P., J. Rutqvist, D. Vasco, J. Garcia, P. F. Dobson, M. Walters, C. Hartline, and A. Borgia (2014), A 3D hydrogeological and geomechanical model of an Enhanced Geothermal System at The Geysers, California, *Geothermics*, *51*, 240–252, doi:10.1016/j.geothermics.2014.01.013.

Klein, F. (2002), User's guide to HYPOINVERSE-2000, a Fortran Program to Solve for Earthquake Locations and Magnitudes, *U.S. Geol. Surv. Open File Rep.*, *2–171*.

Kwiatek, G., K. Plenkers, and G. Dresen (2011), Source parameters of picoseismicity recorded at Mponeng deep gold mine, South Africa: Implications for scaling relations, *Bull. Seismol. Soc. Am.*, *101*(6), 2592–2608, doi:10.1785/0120110094.

Kwiatek, G., M. Bohnhoff, P. Martínez-Garzón, F. Bulut, and G. Dresen (2013), High resolution reservoir characterization using induced seismicity and state of the art waveform processing techniques, *First Break*, *31*(7), 81–88.

Kwiatek, G., F. Bulut, M. Bohnhoff, and G. Dresen (2014), High-resolution analysis of seismicity induced at Berlín geothermal field, El Salvador, *Geothermics*, doi:10.1016/j.geothermics.2013.09.008.

Madariaga, R. (1976), Dynamics of an expanding circular fault, *Bull. Seismol. Soc. Am.*, *66*, 639–666.

Majer, E. L., and J. E. Peterson (2007), The impact of injection on seismicity at The Geysers, California Geothermal Field, *Int. J. Rock Mech. Min. Sci.*, *44*(8), 1079–1090, doi:10.1016/j.ijrmms.2007.07.023.

Majer, E. L., R. Baria, M. Stark, S. Oates, J. Bommer, B. Smith, and H. Asanuma (2007), Induced seismicity associated with Enhanced Geothermal Systems, *Geothermics*, *36*(3), 185–222, doi:10.1016/j.geothermics.2007.03.003.

Martínez-Garzón, P., M. Bohnhoff, G. Kwiatek, and G. Dresen (2013), Stress tensor changes related to fluid injection at The Geysers geothermal field, California, *Geophys. Res. Lett.*, *40*, 2596–2691, doi:10.1002/grl.50438.

Martínez-Garzón, P., G. Kwiatek, M. Ickrath, and P. Bohnhoff (2014), MSATSI: A MATLAB package for stress inversion combining solid classic methodology, a new simplified user-handling and a visualization tool, *Seismol. Res. Lett.*, *85*, 4, doi:10.1785/0220130189.

McGarr, A. (2014), Maximum magnitude earthquakes induced by fluid injection, *J. Geophys. Res. Solid Earth*, *119*, 1008–1019, doi:10.1002/2013JB010597.

McGarr, A., and J. B. Fletcher (2002), Mapping apparent stress and energy radiation over fault zones of major earthquakes, *Bull. Seismol. Soc. Am.*, *92*(5), 1633–1646, doi:10.1785/0120010129.

Moore, J. N., M. C. Adams, and A. J. Anderson (2000), The fluid inclusion and mineralogical record of the transition from liquid to vapor-dominated conditions in the Geysers geothermal system, *Econ. Geol.*, *95*.

Mossop, A., and P. Segall (1997), Subsidence at The Geysers geothermal field, N. California from a comparison of GPS and leveling surveys, *Geophys. Res. Lett.*, *24*, 1839–1842, doi:10.1029/97GL51792.

Oppenheimer, D. H. (1986), Extensional tectonics at The Geysers geothermal area, California, *J. Geophys. Res.*, *91*, 11,463–11,476, doi:10.1029/JB091iB11p11463.

Parotidis, M., S. A. Shapiro, and E. Rothert (2004), Back front of seismicity induced after termination of borehole fluid injection, *Geophys. Res. Lett.*, *31*, L02612, doi:10.1029/2003GL018987.

Percival, D. B., and A. T. Walden (1993), *Spectral Analysis for Physical Applications: Multitaper and Conventional Univariate Techniques*, Cambridge Univ. Press., Cambridge, U. K.

Provost, A.-S., and H. Houston (2003), Stress orientations in northern and central California: Evidence for the evolution of frictional strength along the San Andreas plate boundary system, *J. Geophys. Res.*, *108*(B3), 2175, doi:10.1029/2001JB001123.

Reasenberg, P., and D. Oppenheimer (1985), FPFIT, FPPLOT and FPPAGE: Fortran computer programs for calculating and displaying earthquake fault-plane solutions, *U.S. Geol. Surv. Open File Rep.*, 85–739.

Rothert, E., and S. A. Shapiro (2007), Statistics of fracture strength and fluid-induced microseismicity, *J. Geophys. Res.*, *112*, B04309, doi:10.1029/2005JB003959.

Rutqvist, J., P. F. Dobson, J. Garcia, C. Hartline, P. Jeanne, C. M. Oldenburg, D. W. Vasco, and M. Walters (2013), The Northwest Geysers EGS Demonstration Project, California: Pre-stimulation modeling and interpretation of the stimulation, *Math. Geosci.*, 1–27, doi:10.1007/s11004-013-9493-y.

Schoenball, M., T. M. Müller, B. I. R. Müller, and O. Heidbach (2010), Fluid-induced microseismicity in pre-stressed rock masses, *Geophys. J. Int.*, *180*(2), 813–819, doi:10.1111/j.1365-246X.2009.04443.x.

Schoenball, M., L. Dorbath, E. Gaucher, J. Florian Wellmann, and T. Kohl (2014), Change of stress regime during geothermal reservoir stimulation, *Geophys. Res. Lett.*, *41*, 1163–1170, doi:10.1002/2013GL058514.

Segall, P., and S. D. Fitzgerald (1998), A note on induced stress changes in hydrocarbon and geothermal reservoirs, *Tectonophysics*, *289*(1–3), 117–128, doi:10.1016/S0040-1951(97)00311-9.

Segall, P., J.-R. Grasso, and A. Mossop (1994), Poroelastic stressing and induced seismicity near the Lacq gas field, southwestern France, *J. Geophys. Res.*, *99*, 15,423–15,438, doi:10.1029/94JB00989.

Shapiro, S. A., P. Audigane, and J.-J. Royer (1999), Large-scale in situ permeability tensor of rocks from induced microseismicity, *Geophys. J. Int.*, *137*(1), 207–213, doi:10.1046/j.1365-246x.1999.00781.x.

Shapiro, S. A., E. Rothert, V. Rath, and J. Rindschwentner (2002), Characterization of fluid transport properties of reservoirs using induced microseismicity, *Geophysics*, *67*(1), 212–220, doi:10.1190/1.1451597.

Shapiro, S. A., R. Patzig, E. Rothert, and J. Rindschwentner (2003), Triggering of seismicity by pore-pressure perturbations: Permeability-related signatures of the phenomenon, *Pure Appl. Geophys.*, *160*(5–6), 1051–1066, doi:10.1007/PL00012560.

Stephens, G., and B. Voight (1982), Hydraulic fracturing theory for conditions of thermal stress, *Int. J. Rock Mech. Min. Sci. Geomech. Abstr.*, *19*(6), 279–284, doi:10.1016/0148-9062(82)91364-X.

Terakawa, T., S. A. Miller, and N. Deichmann (2012), High fluid pressure and triggered earthquakes in the enhanced geothermal system in Basel, Switzerland, *J. Geophys. Res.*, *117*, B07305, doi:10.1029/2011JB008980.

Theis, C. V. (1935), The relation between the lowering of the piezometric surface and the rate and duration of discharge of a well using ground-water storage, *Transactions*, *16*, 519–524.

Vasco, D. W., J. Rutqvist, A. Ferretti, A. Rucci, F. Bellotti, P. Dobson, C. Oldenburg, J. Garcia, M. Walters, and C. Hartline (2013), Monitoring deformation at The Geysers Geothermal Field, California using C-band and X-band interferometric synthetic aperture radar, *Geophys. Res. Lett.*, *40*, 2567–2572, doi:10.1002/grl.50314.

Viegas, G., and L. Hutchings (2011), Characterization of induced seismicity near an injection well at the Northwest Geysers geothermal field, California. Geothermal Resources Council Transactions, 35.

Waldhauser, F., and W. L. Ellsworth (2000), A double-difference earthquake location algorithm: Method and application to the Northern Hayward Fault, California, *Bull. Seismol. Soc. Am.*, *90*(6), 1353–1368, doi:10.1785/0120000006.

Waldhauser, F., and D. P. Schaff (2008), Large-scale relocation of two decades of Northern California seismicity using cross-correlation and double-difference methods, *J. Geophys. Res.*, *113*, B08311, doi:10.1029/2007JB005479.

Wiemer, S., and M. Wyss (2000), Minimum magnitude of completeness in earthquake catalogs: Examples from Alaska, the Western United States & Japan, *Bull. Seismol. Soc. Am.*, *90*, 859–869.